CCFE
CULHAM CENTRE FOR FUSION ENERGY

UK Atomic Energy Authority

UKAEA-CCFE-PR(22)51

Qiong Lu1, Chi Zhang, Wei Wang, Shuai Jiang, Lee Aucott, Jun Jiang

Reveal the Viscoplastic Behaviour and Microstructure Evolution of Stainless Steel 316L

Reveal the Viscoplastic Behaviour and Microstructure Evolution of Stainless Steel 316L

Qiong Lu1, Chi Zhang, Wei Wang, Shuai Jiang, Lee Aucott, Jun Jiang

This is a preprint of a paper submitted for publication in
Journal of Nuclear Materials

Reveal the Viscoplastic Behaviour and Microstructure Evolution of Stainless Steel 316L

Qiong Lu[1,2,◇], Chi Zhang[1, ◇], Wei Wang[1], Shuai Jiang[1], Lee Aucott[3], Jun Jiang[1*]

1. Department of Mechanical Engineering, Imperial College London, Exhibition Road, London, SW7 2AZ, UK
2. Powder Metallurgy Research Institute, Central South University, Changsha, 410083, China
3. U~~K Atomic Energy Authority, Culham Science Centre, Abingdon, OX14 3DB, UK~~ United Kingdom Atomic Energy Authority, Culham Centre for Fusion Energy, Culham Science Centre, Abingdon, Oxon, OX14 3DB, UK.

Abstract

Stainless-steel 316L is one of the widely used structural materials in the nuclear industry, because of its excellent corrosion resistance and mechanical properties. However, very few researches can be found on its viscoplastic behavior and microstructure evolution at warm and hot deformation conditions, which hinder the possible application of advanced manufacturing technologies for producing complex parts, such as superplastic forming or hydroforming. The aims of this study are to explore the stainless steel 316L viscoplastic behavior to determine its strain rate sensitivities and to reveal its underlying microstructure evolution; these will allow appropriate manufacturing (forming) technologies and the optimal forming condition to be determined. Hence, isothermal tensile tests at 700°C, 800°C, 900°C, and 1000°C at the strain rates of 0.01 s^{-1} and 0.001 s^{-1} have been carried out. Also, the corresponding microstructure evolution including the grain orientation and geometrically necessary dislocation density have been revealed by electron backscatter diffraction method. The data show the viscoplastic behavior of stainless-steel 316L under various thermomechanical deformation conditions and how the microstructure evolution influences the viscoplastic flow stress.

Keywords: austenitic stainless steel 316L, large grain size, recrystallization, viscoplasticity

◇ The authors contribute equally to this work

*Corresponding author: jun.jiang@imperial.ac.uk

1. Introduction

Using advanced metal forming methods for producing complex-shaped stainless steel 316L (SS316L) parts is highly desirable for future fusion reactor structural components. The SS316L is a member of the austenitic steels which was developed more than three decades ago for fast-breeder reactor applications within the EU countries [1, 2]. Based on its excellent properties, SS316L was selected as the main structure retaining material for Vacuum Vessel and the first wall/shielding blanket component (blanket shield block) in the International Thermo-Nuclear Experimental Reactor (ITER) [3, 4]. The shielding block has drilled coolant channels which need a multi-layer structure and assemble of different subcomponents to achieve the final complex part [5, 6]. This process is challenging and costly, and the assembled larger components are under a higher structural integrity risk due to the presence of many long joints [1]. Thus, using advanced manufacturing methods for producing complex-shaped parts with reduced joints, are highly desirable for future fusion reactor structural components. Warm or hot forming of complex-shaped components using superplastic forming or hydroforming has increasingly been used in recent years due to its numerous advantages [7, 8]. It can produce components with complex geometries, such as the high aspect ratio ribbed structures, in one manufacturing step [9]. Therefore it decreases or completely eliminates the number of sub-components and joining operations [9].

To apply the warm or hot forming techniques in the future fusion reactor structural components, determining the viscoplastic behavior of SS316L and understanding its underlying microstructure evolution are essential. To achieve the optimal formability of the material, a particular processing window *i.e.,* specific ranges of deformation temperature and strain rate needs to be identified [10]. The strain rate sensitivity, determined from the ratio of the stress variation to the strain rate difference, is an important formability indicator [11]. For example, the superplastic state with an elongation typically larger than 300% can be achieved, if the strain rate value is determined ~0.4-0.5 [12]. The lower value of the strain rate sensitivity, the inferior formability of the material becomes. This strain rate sensitivity value is governed by the diffusion process driven microstructure evolution [13-16]. It is found that the underlying grain size evolution is one of the main intrinsic factors, governing the strain rate sensitivity. Also, the grain size plays a vital role in determining the fracture toughness, fatigue, creep and corrosion resistance of the formed components [17]. Hence, it is important to explore the relationship between grain size and various thermal-mechanical conditions [18, 19]. Such a relationship has been extensively studied among AISI 304L stainless steel [20], super-304H austenitic stainless [21], as well as 410 stainless alloys [22]. However, so far, little research has been devoted to investigating the viscoplastic behavior of SS316L, which is one of the most used structural materials for fusion reactors.

The aim of this study is to reveal the viscoplastic behavior and underlying microstructure evolution of SS316L. To obtain the stress-strain curves, eight samples will be hot deformed at various testing temperatures and strain rates: 700°C, 800°C, 900°C and 1000°C, at the strain rates of 0.01 s^{-1} and 0.001 s^{-1}, respectively. Based on these obtained stress-strain curves, the strain rate sensitivity calculation will be undertaken as a function of deformation temperature and strain. Moreover, the underlying grain size, grain orientation and the geometrically necessary dislocation (GND) density will be analyzed by the electron backscatter diffraction (EBSD) technique to provide insights into microstructure evolution.

2. Experimental Methodology

2.1 As-received material and the testing samples

The as-received sample, its preparation for testing and detailed testing procedures are described here. ASTM A240 316L steel rods were provided by Masteel, UK, with a diameter of 20 mm. Its chemical composition is reported in Table 1. Its microstructure was characterized using EBSD, as seen in Fig. 1. Fig. 1(a-b) depicts the grain orientation map by the inverse pole figure (IPF) and preferential orientation distribution, *i.e.,* texture, through the pole figure (PF). The initial microstructure consists of equiaxed grains with little noticeable texture. Also, it confirms the austenitic phase (iron FCC) structure. In these FCC austenitic grains, moderate GND content can be found, as shown in Fig. 1(c). The presences of these moderate GND density points imply that the initial material is likely in a wrought state without heat treatment. Undertaking a statistical analysis of the grain size, the grain size is relatively uniform with a moderate average grain size of ~37 μm, as shown in Fig. 1(d). Moreover, a large fraction of annealing twins exist in the microstructure due to the low stacking fault energy of the 316L [23, 24]. These twin boundaries were identified according to the specific misorientation (60°) with the axis (<111>). The quantitative data of the twinned area and twined grain fraction were calculated and shown in Fig. 1(e). Note that these twin boundaries were excluded from the previous grain size analysis in Fig. 1(d).

Table 1. Nominal chemical composition of SS316L

Element	Fe	C	Mn	Si	P	S	Cr	Ni	Mo	N
Wt.%	Bal	0.08	2	0.75	0.045	0.003	16-18	10-14	2-3	0.1

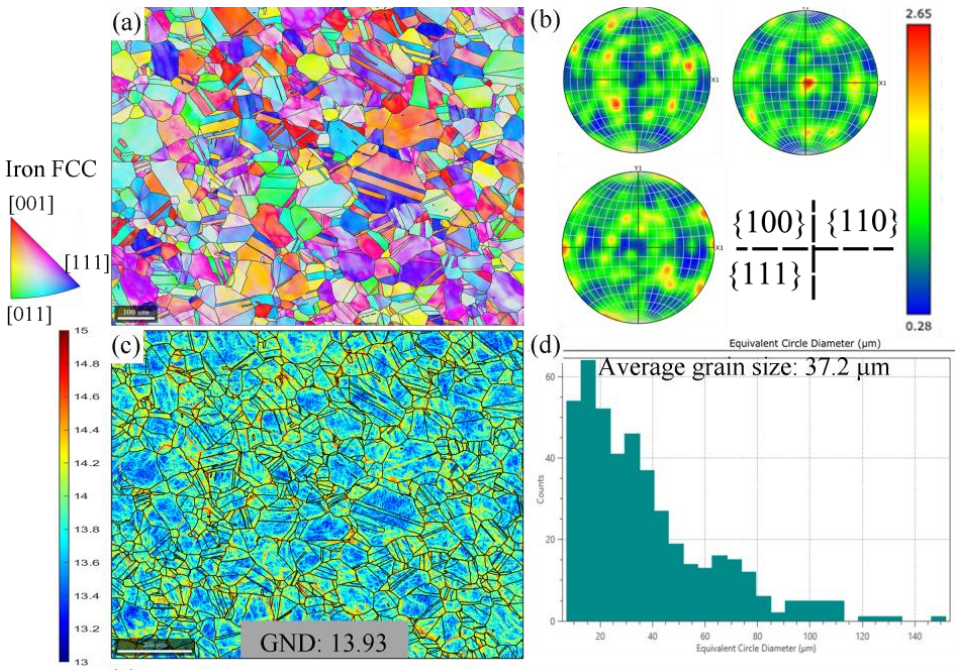

(e) Table 2 The details of twinning

Twinned Grains Count	Twinned Grain fraction (%)	Twinned Grain Area fraction (%)
247	55.88	87.99

Fig. 1. Microstructure of as received SS316L: (a) EBSD IPF images, (b) pole figures, (c) GND density map, and (d) the grain size distribution, (e) annealing twinning information.

These rods were machined using a wire-cut electrical discharge machine, into uniaxial hot tensile testing samples, according to the ASTM E-2448 standard [25], as presented in Fig. 2(a). These machined samples were subjected to the hot tensile test using Instron 3369 thermal-mechanical testing machine (Instron, Boston, MA, USA), as shown in Fig. 2(b). It can operate from room temperature to 1200°C with ± 2°C accuracy using an attached two-halves-split furnace. The pull rods of the machine are equipped with cylindrical bearings at both bar ends: upper and lower. This setup ensures good alignment between the specimen axis and the loading axis. The pull rods were joined to specimen grip boxes using short, double threated link rods. The displacement was measured by an extensometer (CBY-DG 25-5), attached to the gauge region of the specimens.

The testing program is schematically illustrated in Fig. 2(c) that the testing sample was firstly heated to 100°C lower than the designed testing temperature with the heating rate of 10°C per minute; after that, the heating rate was reduced to 3°C per minute to heat the sample to the designed temperature which would minimize the temperature overshooting issue. To ensure the temperature uniformity along the sample, the sample was soaked at the designed temperature for 15 mins prior to the onset of the loading. The loading process was undertaken using displacement control, according to the designed strain rate, until the occurrence of the fracture; then, the sample was furnace cooled to the room temperature. Uniaxial hot tensile experiments were conducted at

two strain rates of 0.01 mm s^{-1} and 0.001 mm s^{-1}, and four temperatures of 700°C, 800°C, 900°C and 1000°C, respectively.

During the hot tensile tests, argon was used as a protective gas to minimize the surface oxidation issue. Software modification and varying crosshead speed were calibrated to obtain a constant strain rate. The optimum temperature, strain rate and strain rate sensitivity index values were determined. Compared to conventional hot tensile testing, this ultra-high temperature, ultra-low strain rate test takes a significantly longer time and is difficult to perform; thus, only one test per test condition was conducted in this study.

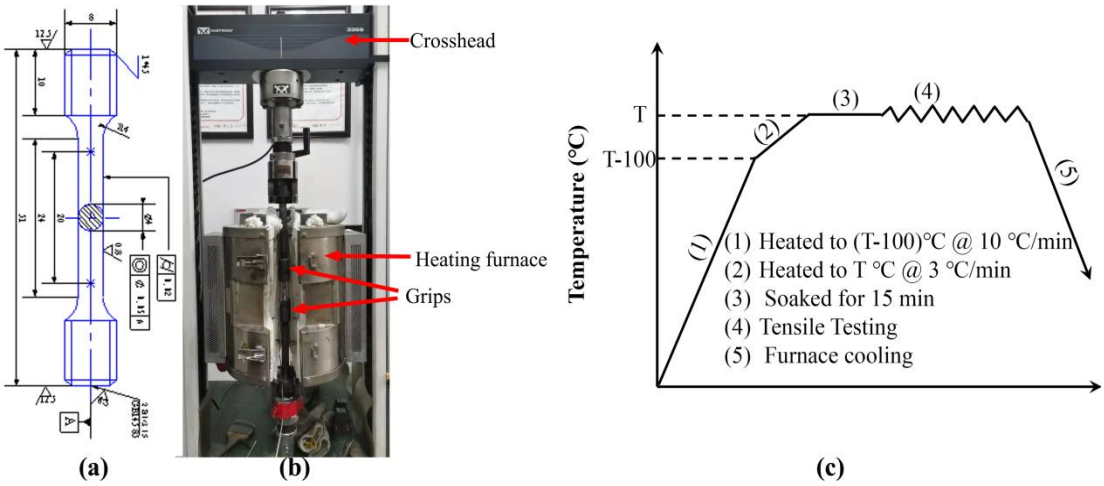

Fig. 2. (a) dimensions of the uniaxial hot tensile specimen, (b) hot tensile testing system used in this study, (c) schematic representation of the thermo-mechanical processing route.

2.2 EBSD characterization

EBSD characterization was conducted on the as-received and deformed samples. The EBSD samples were cut from the grip and gauge regions, as displayed in Fig. 3, to isolate the heat treatment effect from viscoplastic deformation. After that, the EBSD samples were ground down using SiC paper, progressively from 600 to 4000 grits. Subsequently, the ground samples were polished with 1 µm diamond paste and oxide polishing suspension (OPS) polishing for 45 minutes, respectively. These metallurgical prepared samples were placed in a Tescan Clara SEM, in which 20 keV acceleration voltage and 10 nA current were set. Oxford Instrument EBSD system, Symmetry 2, was used to acquire relatively large EBSD maps, *i.e.,* 1400 µm × 1050 µm, with a step size of 2 µm at 150× magnification. The selected map size and step size were due to the balance of the statistically meaningful sampling and containing distinguishable dislocation information (dislocation channels). A smaller area of 600 µm × 435 µm with a finer step size of 0.8 µm was obtained for closer inspection. The EBSD pattern indexing rate is ＞95%, no further data cleaning was undertaken. The grain size and GND density were analyzed using the MTEX toolbox, and the grain boundary was set as 10° misorientation.

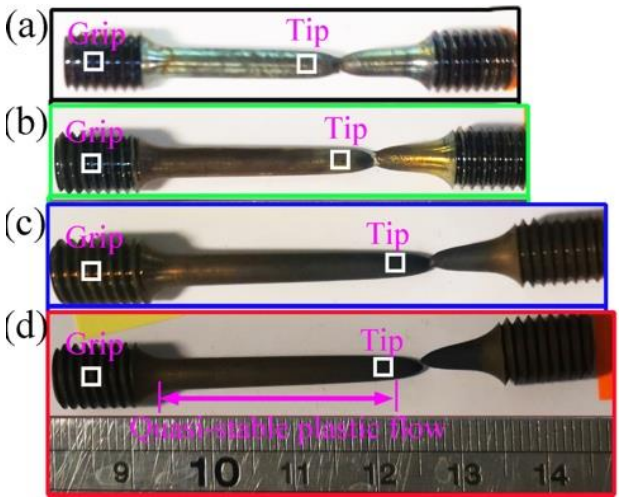

Fig. 3. Macroscopic morphology of specimens after tensile test: (a) 700°C, (b) 800°C, (c) 900°C, (d) 1000°C at the strain rate of 0.01s^{-1}. The highlighted white squares are the selected EBSD regions.

3. Results and discussion

3.1 3.1 Stress-strain behavior

The true stress-strain curves at various temperatures and strain rates are reported in Fig. 4. It can be seen that the flow stress is very sensitive to the change in deformation temperature and strain rates. All curves exhibit peak stress rapidly after the initial hardening. These peak stresses decreased gradually with increasing temperature and decreasing strain rate. At the high strain rate, the peak stress decreases from 361 MPa to 111 MPa from 700°C to 1000°C. At 700°C, the curve displays a steady state after a peak stress, which means that the dynamic softening and hardening reached an equilibrium. As the deformation temperature increases from 800 to 1000°C, the curves exhibit a continuous flow softening regime after the peak stress up, which suggests the predominant softening effects exerted by dislocation recovery, recrystallization or grain boundary sliding [26-28].

The elongation of the specimens generally increases with higher temperature, while the strain rate seems to have little influence on the ductility. The highest elongation of 50% is observed at 1000°C, whereas the lowest one (~20%) is found at the lowest testing temperature of 700°C.

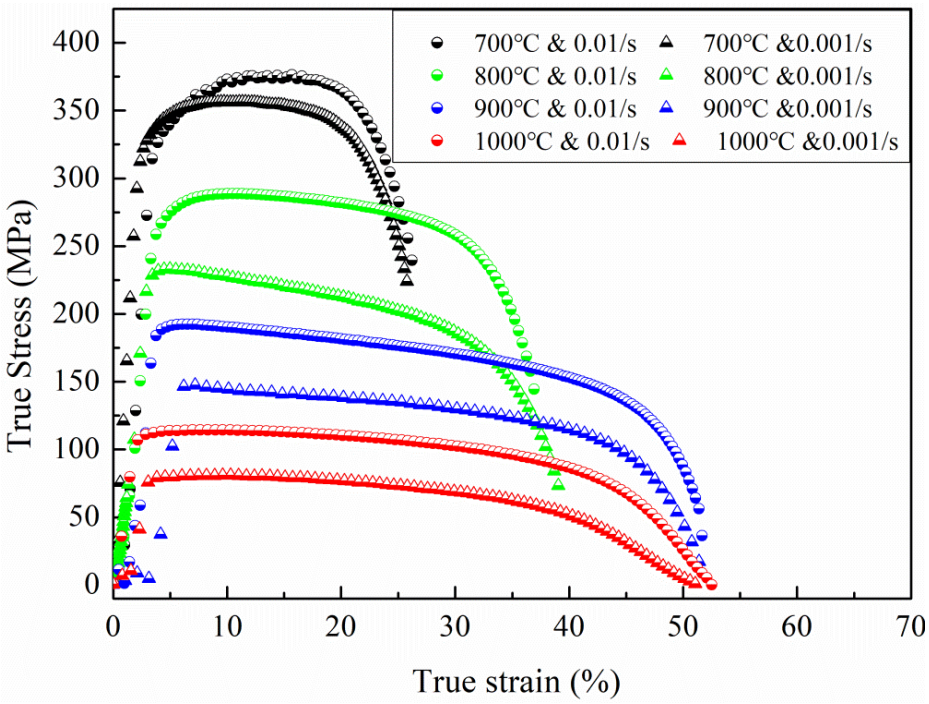

Fig. 4. The effect of temperature and constant strain rates on stress-strain behavior.

The strain rate sensitivity index, m, which is a generally accepted as a formability indicator, was calculated using the following equation [29]:

$$m = \frac{\partial \ln \sigma}{\partial \ln \dot{\varepsilon}} |T, \varepsilon$$

where σ is the flow stress, $\dot{\varepsilon}$ is the strain rate, T is the absolute temperature in kelvin and ε is the true strain.

m-value of 0.33 was achieved at the strain of 45% at 1000°C, which is approximately twice higher than that at its 20% strain. The results were reported in Fig. 5. m increases gradually with the rising temperature. For example, m is determined as 0.03, 0.12, 0.12, and 0.15 at 700°C, 800°C, 900°C, and 1000°C, respectively. Low m values, less than 0.1, indicate low strain rate sensitivity, and hence have the tendency to strain localization and necking, which means poor formability. However, at 1000°C, there is an increasing trend for the strain rate sensitivity, which increased from 0.15 at the strain level of 20% to 0.33 at the strain level of 45%. 0.33 for m is very high, which means that if the microstructure at this state could be maintained as a steady state during the deformation, the elongation of the materials could be considerably large (>300%), since m=0.33 is defined as a superplastic condition in the literature [26, 30]. In a physical sense, it means that the microstructure at this strain level has sufficient diffusion taking place at the grain boundaries, which allows the grain boundary sliding, the predominating mechanism for superplasticity, to occur [31].

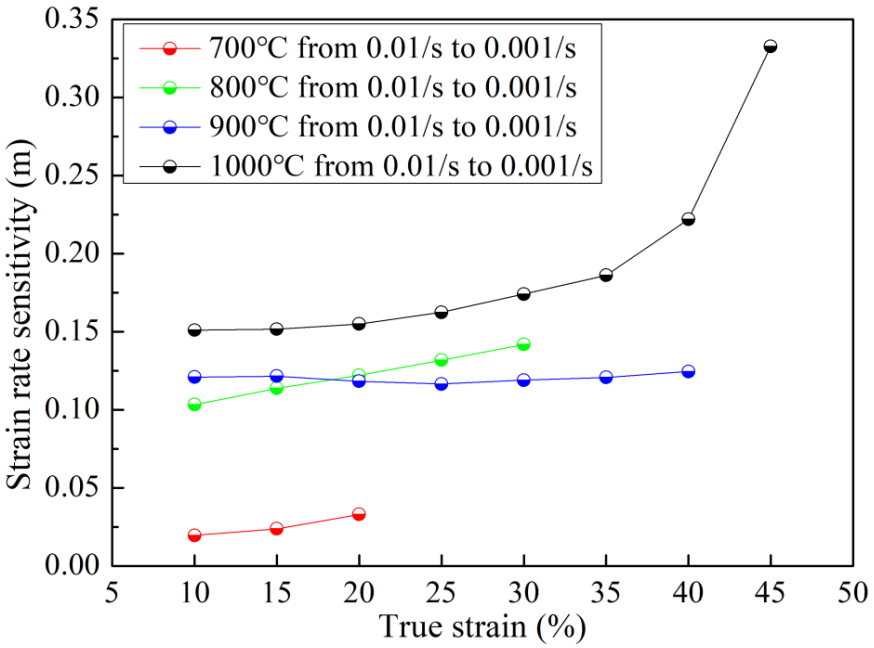

Fig. 5. Strain rate sensitivity evolution with deformation temperature

3.2 Grain evolution

EBSD orientation maps under various deformation temperatures exhibit considerable grain size changes from 700°C to 1000°C, as presented in Fig. 6. Both the high angle grain boundaries and the low angle grain boundaries are highlighted in the maps. The grains are elongated along the vertical axis, which corresponds to the loading axis. The grain sizes of all four conditions are found to be larger than that of the as-received grains. Also, more low angle grain boundaries (LAGB) exist in the higher temperature deformed samples. The grains size initially increased gradually with increasing tensile temperature from about 56.9 μm (which is ~53% larger than that of as-received alloy) at 700°C to 64.1 μm (which is ~72% larger than that of as-received alloy) at 900°C. Whereas, the deformation temperature increased to 1000°C, it is interesting to note that a significant decrease in grain size (42.4 μm, which is ~34% smaller than that at 900°C), due to the occurrence of dynamic recrystallization (DRX). The recrystallized grains can be distinguished by their smaller size (Fig. 6(d)) and their equiaxed shape. Clear necklace microstructures emerged near grain boundaries.

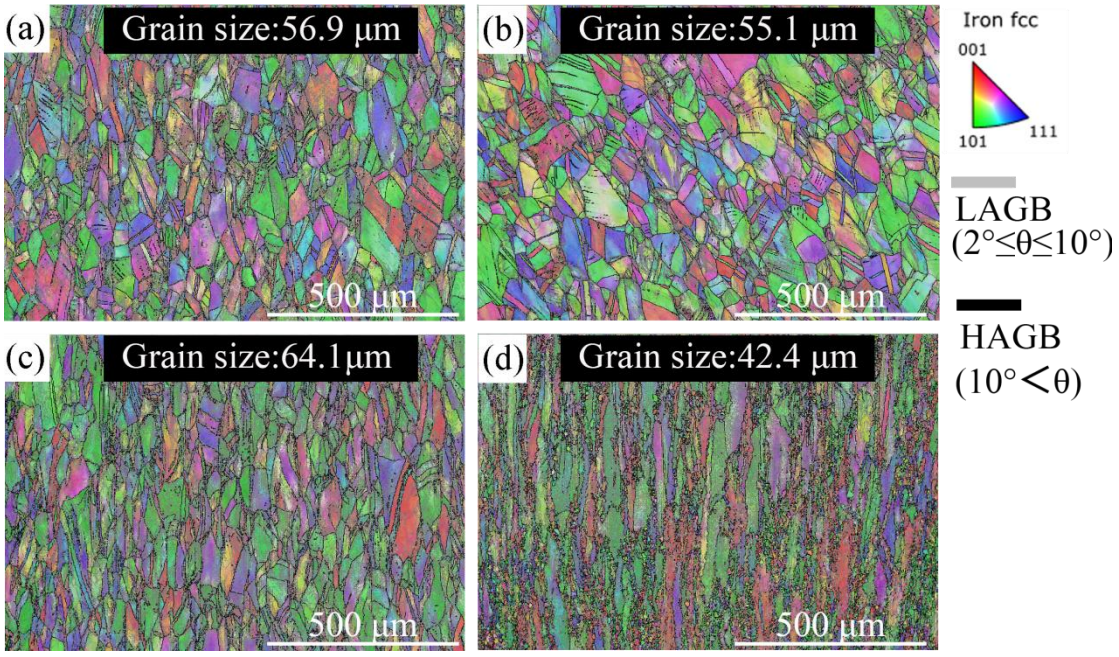

Fig. 6. Grain orientation maps of SS316L deformed at the temperature of: (a) 700℃, (b) 800℃, (c) 900℃, (d) 1000℃, respectively.

The recrystallization was further analyzed using the method of grain orientation spread (GOS) within grains [32]. Identifying the recrystallized grains is challenging, since the recrystallized grains are deformed simultaneously once they are generated. It is often hard to distinguish them from the original grains. Nevertheless, in this study, the recrystallized grains are in their early stage that their size tends to be significantly smaller than the original grains. Also, the recrystallized grains could be formed during the cooling process, *etc*., post deformation recrystallization. Thus, their orientation spread within grains is low. Therefore, it is reasonable to utilize the GOS to distinguish the recrystallized grains.

In this study, the grains with a GOS value below 2.6° were identified as DRXed grains. The grain size and GOS criteria for distinguishing recrystallized grains have been compared, as shown in Fig. 7. The new DRXed grains with equiaxed shapes presented a homogeneous grain size (~15 μm) distribution and the DRX fraction is about 17.5% (as shown in Fig. 7(a)), which is consistent with the cumulative area fraction at GOS smaller than 2.6° (as shown in Fig. 7(b)). These indicate that 2.6° threshold used by GOS to distinguish DRXed is sensible.

In this sample, LAGBs fill the unDRXed region and unDRXed grains exhibited a relatively large size and dramatically elongated (Fig. 6(d)). These LAGBs are formed by the pile-up of dislocations with the same sign. The high content of LAGB indicates the high dislocation density, *etc.,* plastic strain energy stored in the material. As DRXed grains form near the grain boundaries with a necklace structure of equiaxed grains form, and the SS316L has relatively low stacking fault energy, which means its dislocation recovery rate is low. Thus, the current DRX is discontinuous DRX, which is consistent

with previous DRX studies in SS316L [33].

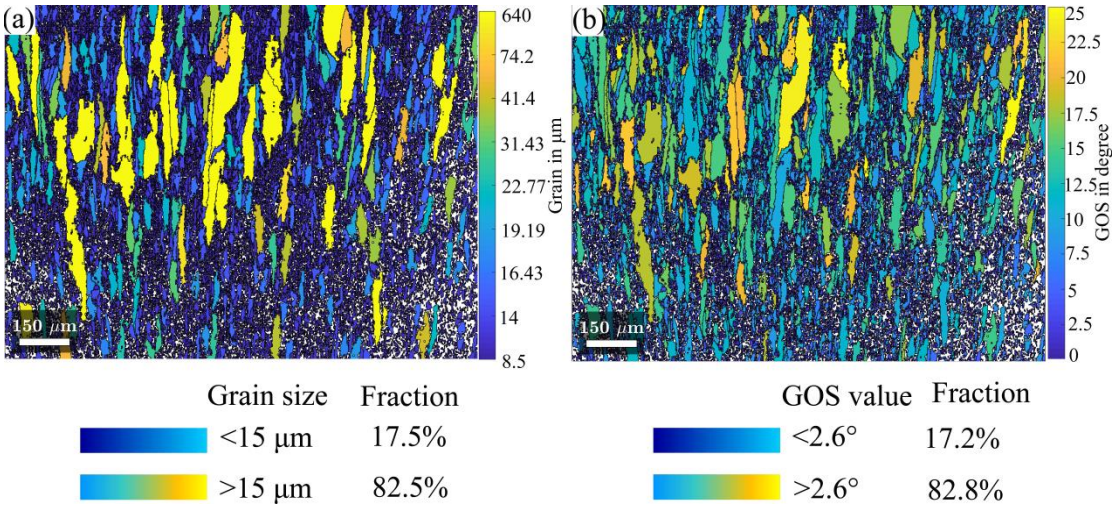

Fig. 7. Identification of recrystallization grains based on grain orientation spread.

As dislocation density is the main driving force for discontinuous DRX [34], to analyze the dislocation change the geometrically necessary dislocation (GND) density, which results in lattice geometrical change and curvature by the presence of dislocations with the same sign, was obtained by measuring the local orientation change from EBSD and further processed using MTEX [35], and the results are shown in Fig. 8.

3.3 GND density evolution

The effects of the static annealing process under various testing temperatures are revealed by checking the GND densities in the grip parts of the sample, which is subjected to static annealing without involving any deformation, are presented in Fig. 8(a-d). It can be inferred that, since the as-received material has large dislocation content, the overall GND density decreases gradually with the increasing annealing temperature, suggesting a more active recovery process as the temperature and diffusion process increase. At 1000°C, as can be seen in Fig. 8(d), a few small grains are dislocation-free, as shown in the dark blue regions, which indicates that static recrystallization has be activated through the increasing thermal energy [13, 36].

It is interesting to see the increase of GND density in the deformed region as a function of increasing deformation temperature. The previous study on hot compression 316L to 50% at various temperatures showed a strong positive correlation between the flow stress and the GND density [37]. However, this trend does not show in the current study. It is less surprising if we consider the various plastic strain levels in the current study that the GND is measured at the end of the test, for which the materials exhibit higher elongation with increasing temperatures. Although there is no significant hardening, the GND density tends to increase with plastic strain. It should be noted that EBSD maps were captured near the fracture tip where the plastic strain and strain rates could be much higher than the nominal ones. In general, at the provided deformation temperature,

the average stored GND contents increased with the increase in plastic deformation [38]. Considering the specimen that deformed at 700°C, the averaged GND density increased from 13.9 to 14.16 at the $\log_{10}$ scale (as shown in Fig. 8(a) and Fig. 8(e)), as the strain increased from 0 to 20%. This trend is consistent at 800°C, 900°C, and 1000°C, by comparing the grip and deformed regions.

Closer examination of the GND structures in Fig. 8 (e-h), one can observe that the GNDs gather near the grain boundaries, especially around the trip junctions, which is consistent with the GND structure formed under the room temperature deformation [39], and most of the high-temperature-induced GNDs also tend to form channel-like structures across the bulk matrix. These channels structured GNDs could be identified from the accumulated red and yellow colors inside the grains. The channels are often parallel with the direction of grain elongation, which is the same with the deformed axis. According to the color difference, we can identify that the GND structure progressively expand along the loading axis and the river-like pattern starts to develop.

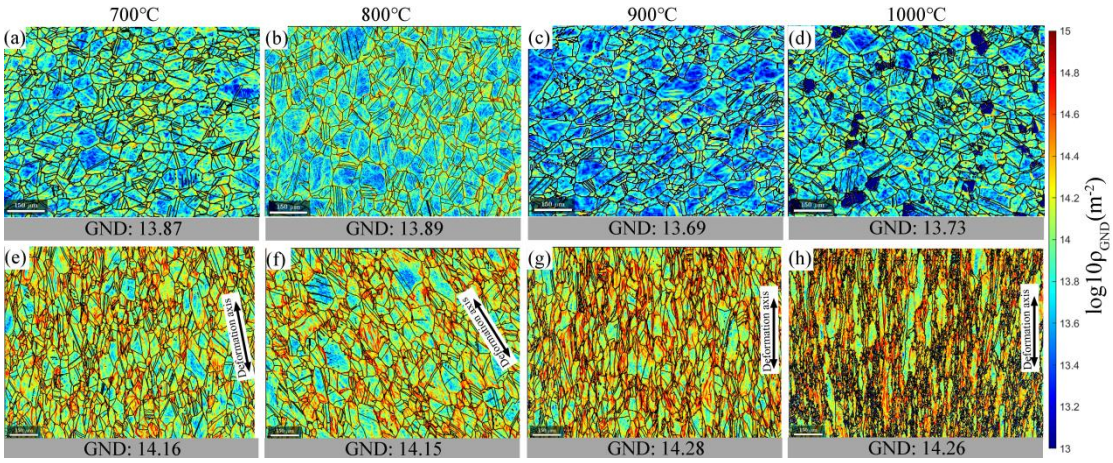

Fig. 8. GND maps of SS316L deformed at 0.01 s^{-1} strain rate and different tensile temperatures. Note that (a), (b), (c), and (d) are grip areas; (e), (f), (g) and (h) are tip areas. The color bar shows GND density in the log_{10} scale of line m^{-2}.

3.4 Dynamic recrystallization and twin boundaries

To provide more insights into the underlying nucleation mechanisms and figure out why most new grains nucleate at grain boundaries, higher spatial resolution EBSD maps were made at the different stages of dynamic recrystallization. As the driving force of the recrystallization is the dislocation density [40], regions with different dislocation density, as shown in Fig. 9(a-c), are selected from the gauge part due to the none uniform deformation. For these three regions, the distances from the fracture tip area are 10 μm, 5 μm, and 2 μm, respectively. The GND density and GOS analyses are undertaken, and the results are presented in Fig. 9(d-i).

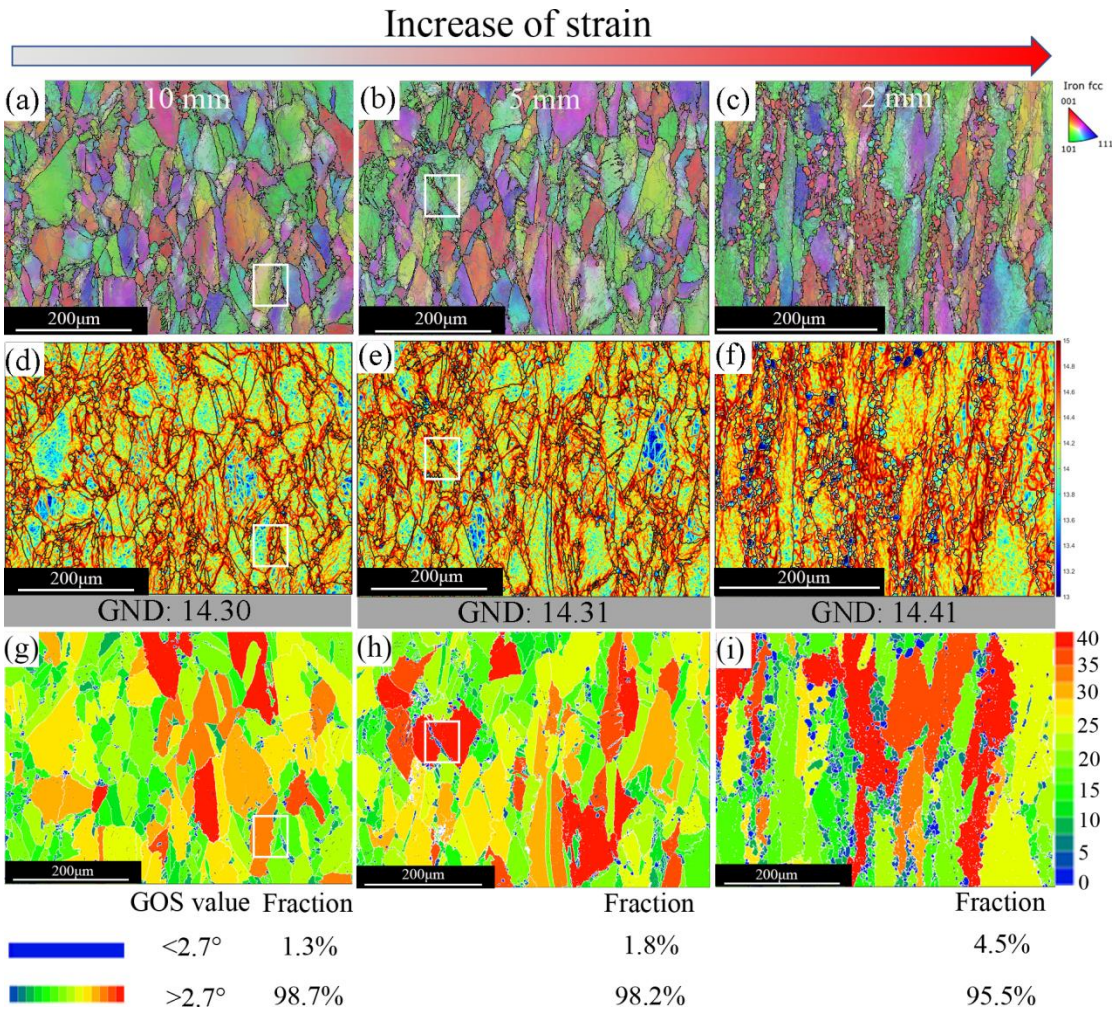

Fig. 9. (a)-(c) EBSD IPF maps of different position deformed at 1000℃ with 0.01 s^{-1}, (d)-(i) their corresponding GND density and GOS maps, respectively.

The recrystallized fraction increases with increasing strain. Some of the regions are highlighted, marked in white squares, in Fig. 9(a), (d), and (g). It can be seen that at the beginning of recrystallization, grain boundaries become serrated due to the dislocation density gradients close to the boundaries and the grain boundary serration is accompanied occasionally by local sub-boundaries formation. With the strain increasing, the deformation twins are formed (as shown in Fig. 9(b), (e), and (h)), which also seem to play an important role in the nucleation mechanism. Twinning induces a change in the boundary misorientation and possibly higher mobility and leads eventually to the grain nucleation. As can be seen on the GOS map (Fig. 10, the magnification of the white box in Fig. 9(b)), the new recrystallized grains, having a low dislocation density (blue color corresponding to a low GOS value, as shown in Fig. 10(b)), are only separated by a twin boundary from the deformed grain. Therefore, it can be concluded that deformation twin boundaries seem a preferential nucleation site for recrystallization happens.

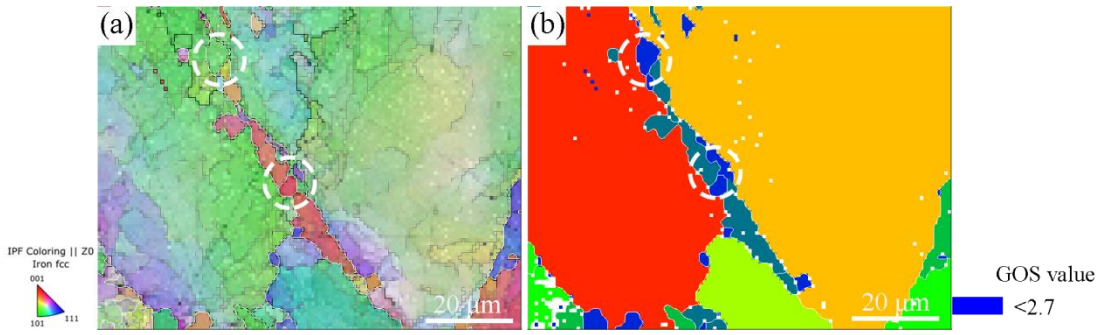

Fig. 10. Grain nucleation at twin boundaries of the deformed grain from the boxed area in Fig. 9(b)

3.5 Viscoplastic mechanism

A schematic illustration of the deformation mechanism evolution during the high temperature tensile test is shown in Fig. 11. At 900°C, the strain rate sensitivity value is ~0.125, which indicates that the deformation mechanism is under diffusional creep [41]. The underlying mechanism is speculated to be driven by vacancy movement along the grain boundaries. The grain boundary perpendicular to the external loading axis is stretched and the grain boundary parallel to the external force axis is compressed. Because the grain boundary itself is the source and annihilation well of the vacancies [42], the formation energy of the vacancies perpendicular to the force axis is low and the number of vacancies is large. However, the grain boundary vacancies parallel to the force axis have higher vacancy formation energy and fewer vacancies, resulting in the formation of certain vacancy concentration difference vacancies in the grain interior flowing in the direction of solid arrows and atoms flowing in the direction of dotted arrows, resulting in plastic deformation with elongation. As the vacancy aggregates form a dislocation, a channel like structured GNDs will be formed within the elongated grains during the high temperature tensile test. At the same time, this deformation mechanism limited the plasticity of the matrix which is consistent with the stress-strain curve and strain rate sensitivity value as shown in Fig. 4 and Fig. 5, respectively.

Increasing the tensile deformation temperature to 1000°C results in both reduced flow stress and increased m value at strain rates of 0.01 s^{-1} and 0.001 s^{-1}, and the corresponding ductility rises from about 26% (700°C with a strain rate of 0.01 s^{-1}) to 53% (1000°C with a strain rate of 0.01 s^{-1}). One advantage of recrystallization is its potential ability to sustain an ultrafine-grained microstructure. The resulting grain refinement then facilitates the sliding of grains, which reduces the effective stress. Besides affecting size, the globular microstructure is beneficial to boundary sliding and grain rotation during superplastic deformation because the elongated morphology is not favorable for the interphase boundary sliding. Thus, the recrystallization during deformation plays a critical role in superplastic deformation.

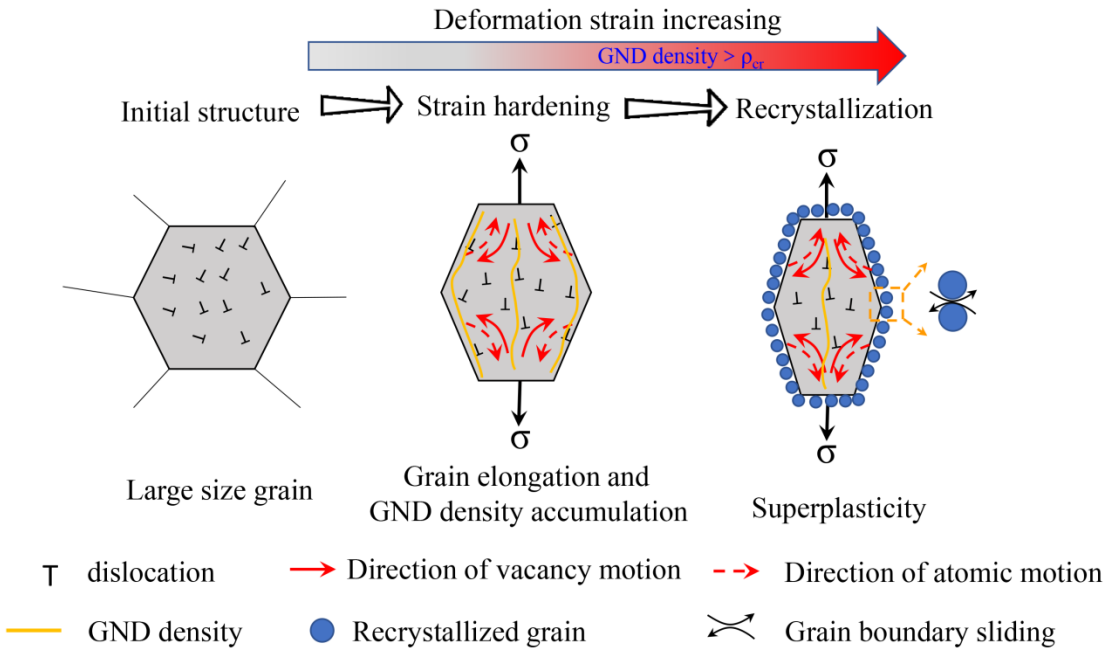

Fig. 11. Schematic illustration of the deformation mechanism evolution during high temperature tensile test

4. Conclusion

The viscoplastic deformation behavior of SS316L has been revealed under the testing temperature range from 700°C to 1000°C and the strain rates of 0.01 s^{-1} to 0.001 s^{-1}. Meanwhile, the underlying microstructure evolution, including grain size and GND density, has been presented. The following main conclusions could be drawn:

(1) Typical viscoplastic behavior has been observed in SS316L that the flow stress decreases with higher temperature and lower strain rates: from ~375 MPa (700°C, 0.01 s^{-1}) to merely 75 MPa (1000°C, 0.001 s^{-1}). At the same time, the ductility of the material increases with higher temperature and lower strain rates from ~22% (700°C, 0.01 s^{-1}) to ~50% (1000°C, 0.001 s^{-1}).

(2) The grain size increases from 37 μm in the as-received material to 64.1 μm in the sample deformed at 900°C. However, the grain size reduces to 42.4 μm at 1000°C due to the occurrence of recrystallization.

(3) Without plastic deformation, the GND density decreased moderately with increasing temperature due to the occurrence of recovery. However, in the deformed regions, GND density increased with plastic strain increased, although the deformation temperature rose simultaneously.

(4) The deformation twin boundaries are found to be the preferential grain nucleation sites, and the vacancy driven deformation mechanism for 900°C and

1000℃ viscoplasticity behavior is proposed.

Acknowledgments

The authors express their sincere gratitude to postgraduate students Famin Tian, Jiaqi Li, Zhe Zhang, Yuzhe Ding, Kaka Cheng from Imperial College London for their valuable ~~advices~~advice. ~~The authors are grateful to the financial support from UKAEA and International Postdoctoral Exchange Fellowship.~~ This work has been part-funded by the EPSRC Energy Programme [grant number EP/W006839/1]. The authors are grateful ~~to~~for the financial support from UKAEA and International Postdoctoral Exchange Fellowship.

References

1. Zhong, Y., et al., *Additive manufacturing of 316L stainless steel by electron beam melting for nuclear fusion applications.* Journal of Nuclear Materials, 2017. **486**: p. 234-245.

2. Mannan, S., et al., *Selection of materials for prototype fast breeder reactor.* Transactions-Indian Institute of Metals, 2003. **56**(2): p. 155-178.

3. Kalinin, G., et al., *Assessment and selection of materials for ITER in-vessel components.* Journal of Nuclear Materials, 2000. **283**: p. 10-19.

4. Ioki, K., et al., *ITER nuclear components, preparing for the construction and R&D results.* Journal of nuclear materials, 2004. **329**: p. 31-38.

5. Giancarli, L., et al., *Test blanket modules in ITER: An overview on proposed designs and required DEMO-relevant materials.* Journal of Nuclear Materials, 2007. **367**: p. 1271-1280.

6. Heinzel, V., et al., *Contributions to the Design of the Electron Cyclotron Launching Upper Port Plug System (ECLUPPS).* 2004.

7. Yagodzinskyy, Y., et al., *Grain refinement processes for superplastic forming of AISI 304 and 304L austenitic stainless steels.* Materials science and technology, 2004. **20**(7): p. 925-929.

8. Lin, J. and T. Dean, *Modelling of microstructure evolution in hot forming using unified constitutive equations.* Journal of Materials Processing Technology, 2005. **167**(2-3): p. 354-362.

9. Jarrar, F., et al. *On the challenges and prospects of the superplastic forming process*. in *Materials Science Forum*. 2018. Trans Tech Publ.

10. Romu, J., et al. *Manufacturing of shaped forms from stainless steels with*

superplastic forming. in *Materials Science Forum*. 2004. Trans Tech Publ.

11. Li, D. and A. Ghosh, *Tensile deformation behavior of aluminum alloys at warm forming temperatures.* Materials Science and Engineering: A, 2003. **352**(1-2): p. 279-286.

12. Sherby, O.D. and J. Wadsworth, *Superplasticity—Recent advances and future directions.* Progress in Materials Science, 1989. **33**(3): p. 169-221.

13. Yasmeen, T., et al., *The study of flow behavior and governing mechanisms of a titanium alloy during superplastic forming.* Materials Science and Engineering: A, 2020. **788**.

14. Sun, Q., G. Wang, and M. Li, *Enhanced the superplasticity in Ti–6.5 Al–2Zr–1Mo–1V alloy by a two-step deformation method.* Materials & Design, 2012. **35**: p. 80-86.

15. Xu, X., G. Wang, and C. Xia, *Stepped superplasticity deformation-induced plastic enhancement of Ti–6Al–1.5 Cr–2.5 Mo–0.5 Fe–0.3 Si alloy.* Materials & Design (1980-2015), 2012. **36**: p. 136-140.

16. Wang, Y., et al., *Hot deformation and processing maps of X-750 nickel-based superalloy.* Materials & Design, 2013. **51**: p. 154-160.

17. Callister Jr, W.D. and D.G. Rethwisch, *Callister's materials science and engineering*. 2020: John Wiley & Sons.

18. Del Valle, J., F. Peñalba, and O. Ruano, *Optimization of the microstructure for improving superplastic forming in magnesium alloys.* Materials Science and Engineering: A, 2007. **467**(1-2): p. 165-171.

19. Horita, Z., et al., *A two-step processing route for achieving a superplastic forming capability in dilute magnesium alloys.* Scripta Materialia, 2002. **47**(4): p. 255-260.

20. Mirzadeh, H., M. Parsa, and D. Ohadi, *Hot deformation behavior of austenitic stainless steel for a wide range of initial grain size.* Materials Science and Engineering: A, 2013. **569**: p. 54-60.

21. Babu, K.A., et al., *Implication of initial grain size on DRX mechanism and grain refinement in super-304H SS in a wide range of strain rates during large-strain hot deformation.* Materials Science and Engineering: A, 2021: p. 142269.

22. Ghadar, S., et al., *A comparative study on the hot deformation behavior of 410 stainless and K100 tool steels.* Materials Science and Engineering: A, 2019. **760**: p. 394-406.

23. Bhattacharjee, P., et al., *Microstructure and texture evolution during annealing of equiatomic CoCrFeMnNi high-entropy alloy.* Journal of Alloys and Compounds, 2014. **587**: p. 544-552.

24. Hertzberg, R.W., R.P. Vinci, and J.L. Hertzberg, *Deformation and fracture mechanics of engineering materials*. 2020: John Wiley & Sons: p. 80.

25. Kumar, M.V., V. Balasubramanian, and A.G. Rao, *Hot tensile properties and strain hardening behaviour of Super 304HCu stainless steel.* Journal of materials research and technology, 2017. **6**(2): p. 116-122.

26. Alabort, E., D. Putman, and R. Reed, *Superplasticity in Ti–6Al–4V: Characterisation, modelling and applications.* Acta Materialia, 2015. **95**: p. 428-442.

27. Manonukul, A. and F. Dunne, *Dynamic recrystallisation in a copper/stainless steel pseudo-two-phase material.* Materials Science and Engineering: A, 2000. **293**(1-2): p. 173-184.

28. Katsas, S., et al., *Dynamic recrystallisation and superplasticity in pure aluminium with zirconium addition.* Materials Science and Engineering: A, 2007. **444**(1-2): p. 291-297.

29. Hedworth, J. and M. Stowell, *The measurement of strain-rate sensitivity in superplastic alloys.* Journal of materials science, 1971. **6**(8): p. 1061-1069.

30. Nieh, T.-G., et al., *Superplasticity in metals and ceramics*. 1997: Cambridge university press.

31. Langdon, T., *A unified approach to grain boundary sliding in creep and superplasticity.* Acta Metallurgica et Materialia, 1994. **42**(7): p. 2437-2443.

32. Hadadzadeh, A., et al., *A new grain orientation spread approach to analyze the dynamic recrystallization behavior of a cast-homogenized Mg-Zn-Zr alloy using electron backscattered diffraction.* Materials Science and Engineering: A, 2018. **709**: p. 285-289.

33. Puli, R. and G.J. Ram, *Dynamic recrystallization in friction surfaced austenitic stainless steel coatings.* Materials characterization, 2012. **74**: p. 49-54.

34. Huang, K. and R. Logé, *A review of dynamic recrystallization phenomena in metallic materials.* Materials & Design, 2016. **111**: p. 548-574.

35. Pantleon, W., *Resolving the geometrically necessary dislocation content by conventional electron backscattering diffraction.* Scripta Materialia, 2008. **58**(11): p. 994-997.

36. Sakai, T., et al., *Dynamic and post-dynamic recrystallization under hot, cold and severe plastic deformation conditions.* Progress in materials science, 2014. **60**: p. 130-207.

37. Liu, Y., et al., *The study of hot deformation on laser cladding remanufactured 316L stainless steel.* Materials & Design, 2021. **212**: p. 110255.

38. Zheng, J.-H., et al., *Quantifying geometrically necessary dislocation density during hot deformation in AA6082 Al alloy.* Materials Science and Engineering: A, 2021. **814**: p. 141158.

39. Jiang, J., T. Britton, and A. Wilkinson, *Evolution of dislocation density distributions in copper during tensile deformation.* Acta Materialia, 2013. **61**(19): p. 7227-7239.

40. McNelley, T., S. Swaminathan, and J. Su, *Recrystallization mechanisms during friction stir welding/processing of aluminum alloys.* Scripta materialia, 2008. **58**(5): p. 349-354.

41. Whittenberger, J.D., *Creep and tensile properties of several oxide dispersion strengthened nickel base alloys.* Metallurgical Transactions A, 1977. **8**(7): p. 1155-1163.

42. Bai, X.-M., et al., *Efficient annealing of radiation damage near grain boundaries via interstitial emission.* Science, 2010. **327**(5973): p. 1631-1634.